Instability of electro-osmotic channel flow with streamwise conductivity gradients

J. Jobim Santos and Brian D. Storey
Franklin W. Olin College of Engineering, Needham, Massachusetts 02492, USA
(Received 8 June 2008; revised manuscript received 5 August 2008; published 31 October 2008)

This work considers the stability of an electro-osmotic microchannel flow with streamwise electrical conductivity gradients, a configuration common in microfluidic applications such as field amplified sample stacking. Previous work on such flows has focused on how streamwise conductivity gradients set a nonuniform electro-osmotic velocity which results in dispersion of the conductivity field. However, it has been known for many years that electric fields can couple with conductivity gradients to generate unstable flows. This work demonstrates that at high electric fields such an electrohydrodynamic instability arises in this configuration and the basic mechanisms are explored through numerical simulations. The instability is unique in that the nonuniform electro-osmotic flow sets the shape of the underlying conductivity field in a way that makes it susceptible to instability. While nonuniform electro-osmotic flow sets the stage, the instability is ultimately the result of electric body forces due to slight departure from electroneutrality in the fluid bulk. A simple stability map is created where two dimensionless numbers can predict system stability reasonably well, even though the system formally depends on six dimensionless groups.

DOI: 10.1103/PhysRevE.78.046316 PACS number(s): 47.20.−k, 47.57.jd

I. INTRODUCTION

One challenge in designing microfluidic devices to perform bioanalytical operations on chip is detection of samples at low concentration. In addition to the development of new instrumentation that can lower detection thresholds, numerous microfluidic systems have been designed which can amplify sample concentration. Amplification techniques such as field amplified sample stacking (FASS) [1] and large volume sample stacking [2] use gradients in fluid electrical conductivity to enhance sample concentration. FASS has received particular attention due to the ease with which it can be integrated into microfluidic devices [3,4].

FASS relies upon using background electrolytes with regions of high and low electrical conductivity in the channel's streamwise direction, an example is shown in Fig. 1(a). Imagine that a channel is started with regions of uniform electrical conductivity and only streamwise conductivity gradients (red indicates high conductivity, blue represents low). An electric potential is suddenly applied across the entire length of the channel. Since the ohmic current down the channel is constant at any streamwise location, most of the potential is dropped across the low conductivity sample region (analogous to three resistors in a series where the middle resistor is the largest). Thus, the electric field is high in the low conductivity sample as shown in Fig. 1(b). In FASS, the sample ions which are to be detected are initially mixed in the low conductivity region. These sample ions are at a much lower concentration than the background electrolytes such that they do not initially influence the overall fluid conductivity. These sample ions will feel an electrophoretic velocity proportional to the local electric field. Sample ions in the low conductivity region will be driven quickly from the region and then slow significantly once they reach the interface with the high conductivity buffer where the electric field is lower. Sample ions that were originally uniformly distributed throughout the low conductivity region will become stacked at the interface. FASS can be implemented with one or two conductivity interfaces where stacking can occur [4], we study the two interface system in this work.

When an electric field is applied, the background electrolyte in Fig. 1(a) will undergo a net electro-osmotic flow down the channel. A solid surface in contact with an electrolyte typically acquires a surface charge and forms an electric double layer, composed of the wall charge and a counterion shielding layer with a thickness on the order of the Debye length. Electro-osmosis results upon the application of an external field parallel to the surface, which sets the diffuse ions of the double layer in motion and induces a motion of

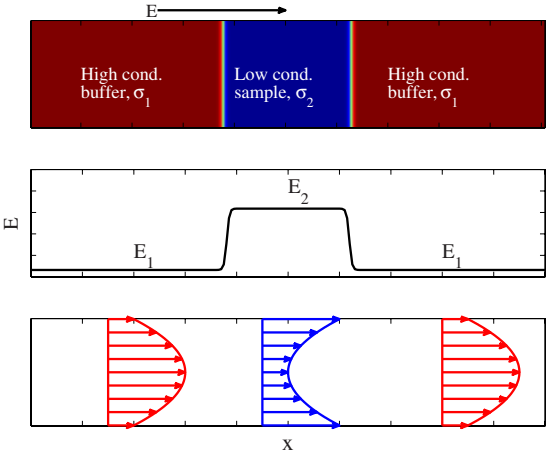

FIG. 1. (Color online) (Top) Schematic of the geometry of interest for this problem. Low conductivity fluid is surrounded by high conductivity buffer. (Middle) When an electric field is applied across the length of this channel, the field is highest in the low conductivity region due to Ohm's law. The result is that the sample ions have a higher electrophoretic velocity in the low conductivity region. All sample ions quickly leave the low conductivity region and stack at the interface with the high conductivity region. (Bottom) The electro-osmotic velocity is highest in the low conductivity sample region. The centerline velocity must then vary inversely with the slip velocity for mass conservation to be obeyed.

the bulk, neutral liquid near the wall [5]. Typical microchannel flows have characteristic scales of order 10 microns or greater and Debye lengths of 10 nm or less so that the electric double layer is confined to a thin layer near the wall. For thin electrical double layers, the electrolyte motion outside of the double layer can be modeled with a slip velocity condition [6]. This slip velocity is proportional to the electric field tangential to the wall.

In a homogeneous fluid when the electric field is constant everywhere, electro-osmotic flow in microchannels has a uniform velocity profile (outside the double layers). In our system where the electric field is nonuniform in the streamwise direction, the electro-osmotic velocity of the low conductivity region is faster than the high conductivity region. The channel's centerline velocity at any streamwise location must vary inversely with the local electro-osmotic slip velocity in order to maintain mass conservation. Thus the nonuniform electro-osmotic flow generates axial pressure gradients [11]. The resulting flow at low Reynolds number will be Poiseuille flow superimposed on a slip flow; as shown in Fig. 1(c). Mass conservation demands that the integral of the velocity profile across the channel (the flow rate) at any streamwise location be constant. Since the bulk flow in the channel has a Poiseuille velocity profile, the interface between high and low conductivity regions will not remain vertical and there will be Taylor dispersion of the fluid sample [5,7]. Taylor dispersion is a flow-induced effect that can act like molecular diffusion in the streamwise direction, only the effective diffusion constant is much greater than molecular diffusion.

This dispersion effect has been recognized since the discovery of FASS and is known to decrease stacking efficiency by quickly broadening the interface between the high and low conductivity regions [1,8]. Due to the importance of FASS, there have been recent numerical and experimental studies on the basic flow and sample dispersion in microfluidic geometries [4,9–11]. In these works, the focus has been on the effect of sample dispersion driven by heterogeneous electro-osmotic slip. There has been little discussion of the role that the electric body force in the nearly electroneutral fluid bulk can have on stability. Further, a number of papers have applied lubrication approximations to develop one-dimensional (1D) models that account for the full flow field [4,7,12]. These models all assume that the modeled flow is stable, though there have been no calculations to test whether this is true.

In recent years, it has been shown that microfluidic flows involving fluids with varying electrical conductivity can be unstable upon application of an electric field [13–17]. The interaction of an applied electric field and fluid conductivity gradients generates charge in the fluid bulk, the applied electric field will exert a force on the charged fluid and electrohydrodynamic (EHD) motions can arise. While these instabilities have only recently been explored in microfluidic applications, it has been known for at least 40 years that electrohydrodynamic motion can occur whenever electric fields are applied to liquids with gradients in their electrical properties [18,19]. The study of instabilities arising from conductivity gradients was pioneered by Melcher and coworkers over 30 years ago [20–23].

Possible instabilities in FASS applications was cited as one of original motivations for studying EHD instabilities in microfluidics [15,16]. Controlling instability in on-chip electrophoresis systems allowed Jung *et al.* [24] to achieve a 1000-fold increase in detection signal. The occurrence of instability in FASS configurations has been discussed but to the best of our knowledge has not been directly studied.

In this work we predict, via numerical simulation, the occurrence of an EHD instability in a flow with streamwise gradients in electrical conductivity. We explore the geometry shown in Fig. 1(a) and expand previous numerical studies that did not account for the electrical body force [10] or limited the parameter regime to cases such that instability would not be observed [9]. Much of the previous work on FASS has focused on the transport and dispersion of the sample ions, in this work we will only study the stability of the background electrolyte. We will show that instability arises from bulk conductivity gradients which are set up by the flow field resulting from the streamwise variation of electro-osmosis. Using our simulations, we will explore the basic mechanism of such instabilities. While many of our conclusions are based on simplified two-dimensional simulations, we show that the basic effect is robust and the instability occurs in three-dimensional simulations as well. Finally, we develop a simple criterion that can inform whether or not stability is likely given the system parameters.

II. FORMULATION

In an earlier work, a set of governing equations suitable for the study of electrokinetic instabilities in microchannels was developed [15]. The foundation of these governing equations are conservation of mass for a two species symmetric electrolyte solution, Poisson's equation for the electric field, conservation of mass for an incompressible liquid, and conservation of momentum including the body force due to an electric field. The general ion transport equations [5] for a dilute, symmetric, monovalent, binary electrolyte (such as KCl in water) can be written as

$$\frac{Dc^+}{Dt} = \nabla \cdot (D \nabla c^+ + \omega F c^+ \nabla \Phi), \tag{1}$$

$$\frac{Dc^-}{Dt} = \nabla \cdot (D \nabla c^- - \omega F c^- \nabla \Phi). \tag{2}$$

Here, c^+ is the concentration of positive ions, c^- is the concentration of negative ions, Φ is the electric potential, D is the diffusivity, ω is the mobility, and F is the Faraday constant. Further, $D/Dt=(\partial/\partial t+\mathbf{v}\cdot\nabla)$, is the material derivative where $\mathbf{v}$ is the velocity field. The right-hand sides of Eqs. (1) and (2) represent the divergence of the ion flux which is composed of molecular diffusion and electromigration.

Our reduced equations make the electroneutrality assumption which states that the difference in cationic and anionic concentrations is small compared to the background concentration, namely $c^+ \approx c^- \approx c$. This assumption is well justified in the fluid bulk outside the very thin electric double layers that form at the channel walls [15]. Using electroneutrality, one can add and subtract Eqs. (1) and (2) to readily obtain

$$\frac{Dc}{Dt} = \nabla \cdot (D \nabla c), \tag{3}$$

$$0 = \nabla \cdot (c \nabla \Phi). \tag{4}$$

Since the electrical conductivity is proportional to the total ionic concentration (under the assumption of a symmetric electrolyte) we can replace the concentration c with the electrical conductivity σ.

Even though we have made the electroneutrality assumption, the slight imbalance in $c^+ - c^-$ yields sufficient charge that the electrical body force in the fluid bulk must be considered [15]. Equations (3) and (4) are therefore coupled to the mechanical problem through the addition of a body force in the incompressible Navier-Stokes equations. To close the problem, Poisson's equation for the electric potential is used to compute the charge density in the fluid bulk from the electric potential. Our complete equation set is therefore

$$\frac{D\sigma}{Dt} = D\nabla^2\sigma, \tag{5}$$

$$\nabla \cdot (\sigma \nabla \Phi) = 0, \tag{6}$$

$$\epsilon \nabla^2 \Phi = -\rho_E, \tag{7}$$

$$\nabla \cdot \mathbf{v} = 0, \tag{8}$$

$$\rho \frac{D\mathbf{v}}{Dt} = -\nabla p + \mu \nabla^2 \mathbf{v} - \rho_E \nabla \Phi. \tag{9}$$

Here, ϵ is the permittivity of the buffer, ρ_E is the charge density, ρ is the buffer liquid density, p is the pressure, and μ is the liquid viscosity. Equations (5)–(9) represent the conservation of conductivity, current continuity ($i = \sigma \nabla \Phi$), Poisson's equation for the electric potential, conservation of mass for an incompressible fluid, and conservation of momentum, respectively. Details on the applicability of Eqs. (5)–(9) and a more rigorous derivation can be found in the literature [15]. The brief derivation we have provided above is meant to be more illustrative than rigorous.

To nondimensionalize the problem we use the following scales: $[x,y,z] = [L,H,H]$, $[u,v,w] = U_{ev}$, $[t] = H/U$, $[\Phi] = E_o H$, $[\rho_E] = \epsilon E_o / H$, $[\sigma] = \sigma_o$, $[P] = \mu U / L$, where H is the height of the channel, L is the length, E_o is the applied electric field, σ_o is the low conductivity, and the characteristic velocity, $U_{ev} = \epsilon E_o^2 H / \mu$, represents the balance between the viscous and electrical forces. This scaling yields the following equation set:

$$\frac{D\sigma}{Dt} = \frac{1}{\mathrm{Ra}} \nabla^2 \sigma, \tag{10}$$

$$\nabla \cdot \sigma \nabla \Phi = 0, \tag{11}$$

$$\nabla \cdot \mathbf{v} = 0, \tag{12}$$

$$\mathrm{Re} \frac{D\mathbf{v}}{Dt} = -\nabla P + \nabla^2 \Phi \nabla \Phi + \nabla^2 \mathbf{v}, \tag{13}$$

where the Reynolds and Rayleigh number are, respectively, defined as

$$\mathrm{Re} = \frac{\rho U_{ev} H}{\mu}$$

and

$$\mathrm{Ra} = \frac{U_{ev} H}{D}.$$

Note that the Rayleigh and Reynolds number are related through the Schmidt number; $\mathrm{Ra} = \mathrm{Re}\,\mathrm{Sc}$, where $\mathrm{Sc} = \rho D / \mu$ and is a property of the fluid. Alternate scalings have been used and these are reviewed by Posner and Santiago [17].

It is important to note that Eqs. (10)–(13) are only valid for the bulk fluid region outside the electric double layer (EDL). This assumption is valid since the typical microchannel dimensions, ~ 10 μm, are much greater than the typical double layer thicknesses, ~ 10 nm. The electric double layers are accounted for through the tangential boundary conditions on velocity with the standard Helmholtz-Smoluchowski slip formula [5]. The flow at the solid walls is bounded by a slip plane which excludes the EDLs of the system and at which the electro-osmotic velocity is directly proportional to the local electric field,

$$\mathbf{v} \cdot \mathbf{t} = -R_v \zeta \nabla \Phi \cdot \mathbf{t}, \tag{14}$$

where ζ is the dimensionless ζ-potential and $R_v = U_{eo} / U_{ev}$ is the ratio of the characteristic electro-osmotic velocity to electroviscous velocity. The electro-osmotic velocity is given by the Helmholtz-Smoluchowski formulation

$$U_{eo} = \frac{\epsilon E_o \zeta_R}{\mu}. \tag{15}$$

Using these definitions, R_v may be also interpreted as the ratio of the ζ-potential to the applied potential, i.e., $R_v = (\epsilon E_o \zeta_R / \mu)(\mu / \epsilon E_o^2 H) = \zeta_R / (E_o H)$. The remaining boundary conditions are that the normal components of velocity, electric field, and conductivity gradient vanish at solid walls.

It is experimentally observed that electro-osmotic velocity depends upon the fluid conductivity [25]. For this work, we adopt the empirical correlation $\zeta = (\sigma / \sigma_R)^{-1/3}$ where σ_R is a reference conductivity at which the dimensional ζ-potential becomes $\zeta = \zeta_R$ [15,25].

The geometry of interest is shown in Fig. 1(a). The configuration starts with a low conductivity sample surrounded by a high conductivity buffer with a vertical, diffuse interface. Initially there are only axial conductivity gradients. We assume periodic boundary conditions in the x direction such that the sample is continuously traveling around a "ring." As we will show, the flow instability is confined to the low conductivity region and the assumption of periodicity is therefore unimportant to our basic result. Of course, in later studies if one wants to directly compare experiments to calculations, an assumption of periodicity may not be appropriate depending upon the experimental arrangement. In this

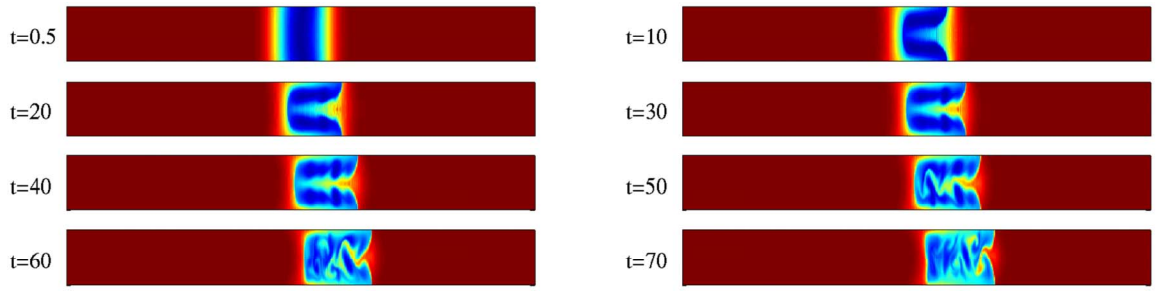

FIG. 2. (Color online) Snapshots of the conductivity field during FASS instability. Parameters are: Ra=2160, R_v=0.056, Re=1.08, γ=10, and δ=0.1. In time, the snapshots move from left to right, then down. The dimensionless parameters correspond to E_o=25 000 V/m, H=50 μm, ζ=0.07 V, and $D=5\times10^{-10}$. The other physical parameters are taken as typical of an aqueous solution. The color bar is set such that red corresponds to σ=10 and blue corresponds to σ=1. The light colored regions correspond to intermediate values of the conductivity and can be used to easily visualize the interface between high and low conductivity fluids. Given the high Rayleigh number, the conductivity field acts as a tracer to visualize the flow.

work we will consider both two-dimensional (2D) and three-dimensional (3D) versions of the geometry shown in Fig. 1.

The equations are solved numerically using Fourier-Chebyshev spectral methods and details on the numerical methods can be found in Ref. [26]. The basic numerical scheme has been used in several previous works by Storey and co-workers [7,15,26–28]. In addition to performing standard numerical tests as discussed in [26], we have also validated our codes against independent linear stability analysis [15,26,28] and show that our full nonlinear simulations agree with analytical depth averaged models which are valid under limits of very thin channels [7,27].

The above formulation depends upon five dimensionless numbers Ra, Re, R_v, $\gamma=\sigma_{\text{high}}/\sigma_{\text{low}}$, and $\delta=H/L$. Further, one can vary the initial condition by changing the length of the sample relative to the channel length introducing a sixth dimensionless parameter. Since the Reynolds number is typically small it does not play a significant role in the problem.

III. RESULTS

A. 2D unstable flow field

We begin by showing the basic mechanism of the instability in Fig. 2. Figure 2 shows snapshots of the conductivity field to demonstrate the onset of electrohydrodynamic instability; the parameters are given in the caption. In these simulations we are assuming that the channel is two dimensional and that the channel depth is infinite. It is clear from the images of the conductivity field at times t=50, 60, and 70 that unstable flow and mixing occurs inside the low conductivity sample. Recalling Eq. (10), we see that the conductivity evolves according to a classic convection-diffusion equation. Since molecular diffusion is quite slow, Ra=2160, the conductivity field effectively acts as a tracer that allows us to visualize the flow. The images of the unstable conductivity field in the sample region contrasts with previous simulations at low electric fields (or neglecting body forces) where the conductivity field remains more regular and symmetric about the channel centerline, as at t=10 [7,9,10].

The mechanism of the instability is as follows. The electro-osmotic slip velocity at the wall is proportional to the electric field tangential to the wall. In the low conductivity sample the electric field and thus the electro-osmotic slip is higher than in the high conductivity buffer. The slip velocity at the leading edge in the sample begins to overtake the buffer causing the conductivity to "pile-up" in a shocklike structure at the wall. The sharpening of the conductivity gradient at the wall of the sample's leading edge is easily seen as time progresses from the first frame when the electric field is suddenly applied to t=30. The result is a narrow region with a very large gradient in the x velocity. Since $\partial u/\partial x$ is large and negative at the location of the "shock," then $\partial v/\partial y$ is large and positive at the wall in order to maintain incompressibility. A large vertical velocity should be expected at the shock location aimed toward the middle of the channel. At the trailing edge of the sample, the situation is reversed. At the trailing edge, $\partial u/\partial x$ is positive at the wall, therefore $\partial v/\partial y$ is negative in order to maintain incompressibility. A vertical velocity aimed toward the wall should be expected at the trailing edge.

Together, the behavior of the vertical velocity at the leading and trailing edge acts to circulate high conductivity fluid through the centerline of the low conductivity sample. At low electric fields these flow patterns and circulation are very regular [7,9]. A strong "shock" structure and nonlinear flow only exist when the electric field is sufficiently high.

As time progresses, this circulation within the sample region sets up a configuration where the sample consists of a thin high-conductivity center along the streamwise direction. This configuration of a conductivity gradient orthogonal to the applied electric fields is known to be unstable from previous work [15,17,26]. The instability seen in the sixth and seventh frames of Fig. 2 are consistent with experiments of Posner and Santiago [17]. The images show that once the flow becomes unstable, that a well-mixed flow can be found inside the low conductivity region. Unstable flow is only observed in the sample where the electric field and electric body forces are sufficiently high. Since the Reynolds number is low, the flow is confined to the low conductivity sample and the instability does not spread to the high conductivity buffer.

Figure 3 shows the conductivity field at different electric fields and at the same dimensionless time, t=50. Here we

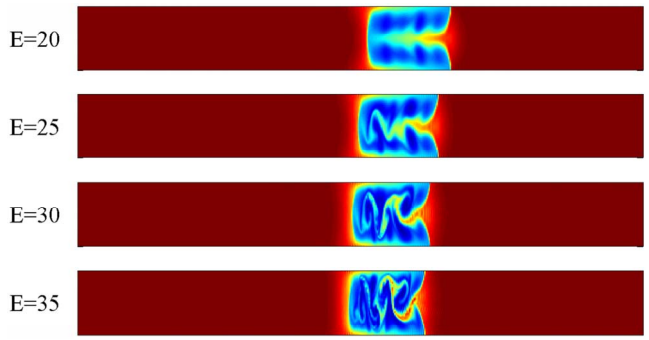

FIG. 3. (Color online) Snapshots of the conductivity field during FASS instability for different electric fields. The parameters are the same as Fig. 2 only the electric field is varied from E_o = 20 000 V/m to E_o = 35 000 V/m from top to bottom. The applied electric field in kV/m is denoted in the figure. The snapshots are taken at the same dimensionless time, t = 50.

can see the motion within the sample gaining a more chaotic appearance as the electric field increases. Further, we can see from this view that the instability is happening quicker relative to the electro-osmotic time. As the field increases the sample has traveled less distance before it is overwhelmed by instability, even though the electro-osmotic velocity increases with electric field. This effect is due to the fact that the electroviscous time, H/U_{ev}, scales with E_o^2 and the electro-osmotic time, H/U_{eo}, scales with E_o.

This channel flow becomes unstable only when the applied electric field is above some threshold. In previous works [13,15,16], the onset of electrohydrodynamic instability was computed using analytical means. In those studies, the conductivity field could be assumed stationary. In this configuration, the conductivity field is set by a transient 2D electro-osmotic flow. In Fig. 2 it is clear that the shape and width of the sample region are rapidly evolving due to the heterogeneous electro-osmotic flow even before instability sets in. Note the change from the initial condition to the conductivity field at t = 10. Initially the conductivity gradients are only aligned with the electric field similar to the work of Baygents and Baldessari [13]. After a short time the conductivity field takes on a 2D shape and there are gradients in both the streamwise and spanwise directions. While it would be possible to use analytical means to study the stability of the initial condition, the initial conductivity field does not remain once the electric field is turned on. After a very short time the electro-osmotic flow deforms the sample into a complex 2D shape. Taylor dispersion continues to cause the width of the sample region [1,7,8] to grow, reducing the overall conductivity gradients and susceptibility of the configuration to instability. Thus, instability must occur on a time scale fast relative to the time scale for Taylor dispersion.

Due to all of these complexities, an analytical method for determining a "true" stability threshold is not possible and we use our 2D simulation to predict system stability. We observe when the flow is stable, there is symmetry about the channel centerline and therefore the vertical velocity is zero at this location. It can be seen in Fig. 2, that when the flow is unstable there is mixing across the centerline within the low

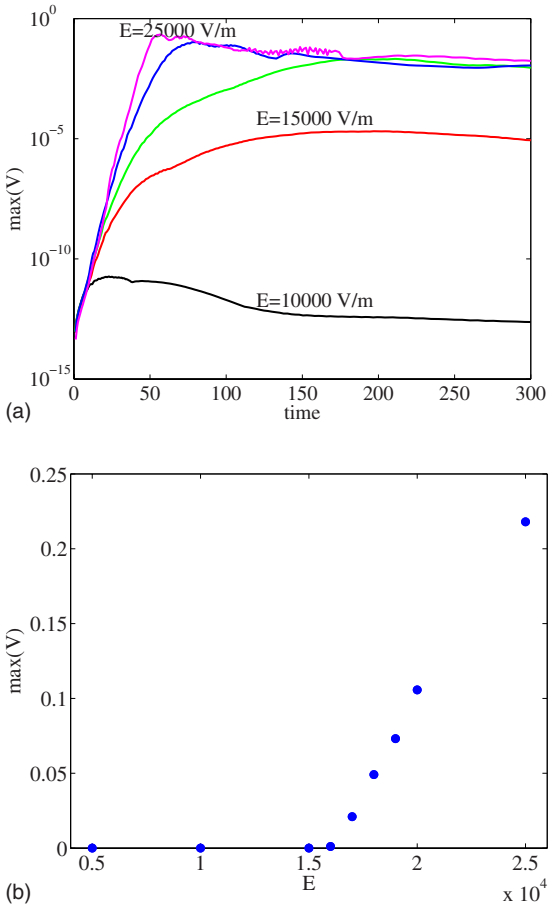

FIG. 4. (Color online) (a) Maximum dimensionless vertical velocity along the channel centerline as a function of time for different electric fields; E_0 = 10 000, 15 000, 17 000, 20 000, and 25 000 V/m from bottom to top. (b) Maximum dimensionless centerline vertical velocity achieved over the course of the run as a function of electric field. The other dimensional parameters are the same as in Fig. 2.

conductivity region. Therefore, we use the maximum nondimensional vertical velocity along the channel centerline as a measure of system stability.

An example of this stability measure for a given geometry is shown in Fig. 4(a). Here we show the maximum dimensionless vertical velocity along the centerline as a function of time for runs with increasing electric field. At low fields (E = 10 000 V/m) we find that the centerline velocity remains so low as not to be well distinguished from numerical roundoff error (10^{-11}). At moderate fields (E_0 = 15 000 V/m), we see an initial exponential growth of the centerline vertical velocity, a maximum of 10^{-5} is reached followed by a slow decay. In these cases, the low conductivity region is linearly unstable at early times. However, the instability growth rate is slow relative to Taylor dispersion which acts to decrease the overall conductivity gradients. The maximum magnitude of the instability is thus too small to be observed in the simulated conductivity fields. A similar effect was noted in Lin *et al.* [15], however in their case it was molecular diffusion of the initial conductivity gradient that could stall the instability. At high fields, we start to see that the instability

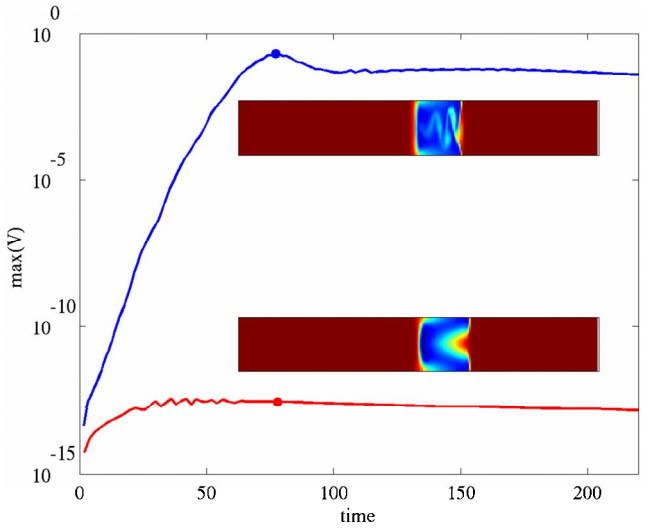

FIG. 5. (Color online) Maximum dimensionless vertical velocity along the channel centerline as a function of time with (upper curve) and without (lower curve) the body force term in the equations. The inset snapshots of the conductivity field are taken where the dot is located, $t=75$. Parameters in both cases are: Ra=880, $R_v=0.0311$, Re=0.88, $\gamma=10$, and $\delta=0.1$.

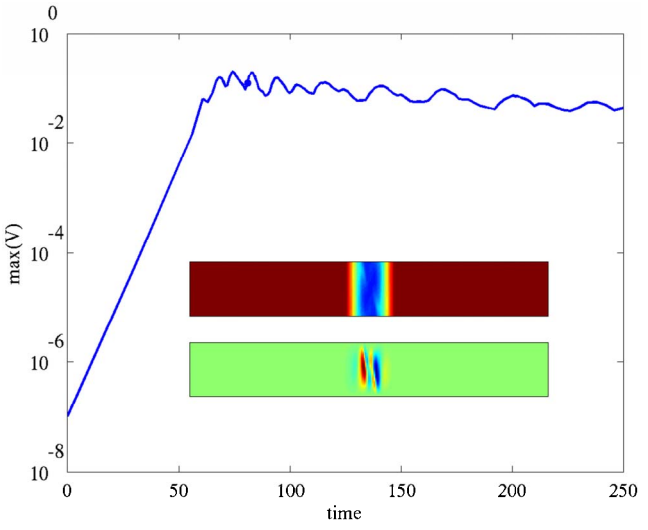

FIG. 6. (Color online) Maximum dimensionless vertical velocity along the channel centerline as a function of time for the case with no electro-osmotic flow. Parameters are the same as Fig. 2 only the electric field is reduced to $E_o=10\,000$ V/m. The inset snapshots show the conductivity field (top) and vertical velocity field (bottom) at $t=75$.

grows quickly relative to the overall rate of sample dispersion. In these cases the velocity increases until a maximum is hit when the instability grows to the size of the system. This behavior is clearly seen in the curve associated with $E_0=25\,000$ V/m. Note that the initial growth rates in dimensionless form collapse to a single curve under the electroviscous scaling as was observed by Lin *et al.* [15]. In all cases, the instability will decay as time progresses and dispersion eventually alleviates the conductivity gradients that drive the flow.

At high electric fields, the maximum vertical velocity at the centerline shows some small scale fluctuations in addition to the longer term growth and decay. Given the highly nonuniform flows that are apparent in the conductivity images of Fig. 2, it is not surprising that there should be some fluctuating component on top of the long time scale growth and decay. We emphasize that we can attribute the small scale fluctuations to unsteady "eddies" within the low conductivity region that are well resolved by our direct numerical simulation.

In Fig. 4(b) we show the maximum dimensionless centerline vertical velocity reached at any time during the entire simulation as a function of electric field. This view allows us to identify a critical electric field for a given set of parameters by extrapolating the computed points to the intercept where $\max(V)=0$. In the case of Fig. 4, we estimate the critical field to be 16 000 V/m.

That the stability is due to electric body forces in the fluid bulk is easy to confirm by "turning off" this term in the simulation. In Fig. 5, we show the dimensionless vertical velocity and conductivity field snapshots for a case with and without the electric body force; all parameters are otherwise the same in the two cases. It is clear that the centerline vertical velocity grows exponentially in the presence of the body force and the snapshot clearly shows an unstable flow. Without the body force, we see the conductivity field is highly nonlinear. The sharp "shocklike" structure still exists at the wall where we have very high gradients in the electrical conductivity. While the conductivity field is highly deformed, the flow remains symmetric about the center line. The centerline vertical velocity never grows in magnitude beyond numerical roundoff error. We note that the case with no body force shows centerline vertical velocities on the order of 10^{-12} (relative to significant vertical velocities at the wall) and therefore the trend should be considered as effectively zero; the flow is symmetric about the center line. While we demonstrate only one case here, we checked different parameters and never observed instability without the electric body force active.

That the flow is dramatically influenced by electro-osmotic flow can be demonstrated by running the simulation with zero ζ-potential and thus no electro-osmotic slip. In this case, there is still a potential electrohydrodynamic instability [26], however the nature is very different. In Fig. 6, we show the maximum centerline velocity as a function of time and associated snapshots of the conductivity field and the vertical velocity field. It is hard to observe much effect by only looking at the conductivity field, however the velocity field clearly shows an unstable flow. In this case with no electro-osmosis, there is only a single unsteady "eddy" inside the low conductivity sample. The unstable flow in the sample is qualitatively different than the cases with electro-osmosis.

The single eddy inside the sample results in the appearance of more unsteadiness in the flow. For example, the time history of the maximum vertical velocity along the centerline in Fig. 6 shows more fluctuation than seen in Fig. 4(a). This difference is simply due to the fact that our measure, the maximum vertical velocity along the centerline, has both local and average properties. We would expect to see that a local measurement of the velocity would be highly unsteady,

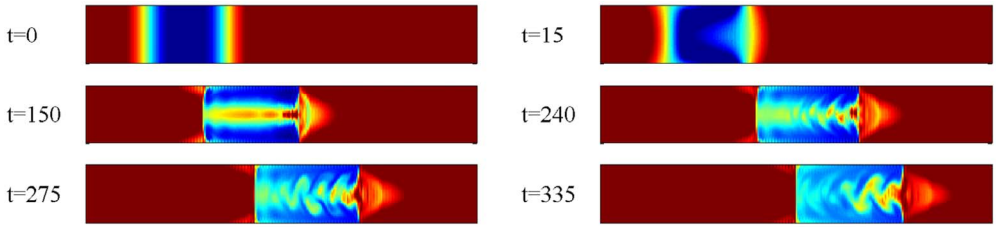

FIG. 7. (Color online) Snapshots of the conductivity field with a 3D simulation in a square channel. The parameters are E_o =35 000 V/m, H=50 μm, ζ=0.07 V, $D=5\times10^{-10}$, γ=10, and δ=0.1. In time, the snapshots move from left to right, then down.

whereas an average measure (such as the total kinetic energy in the flow) would evolve more gradually. When there are many eddies in the sample region [as in Fig. 4(a)], a maximum value taken over the entire centerline in a sense averages over many eddies and thus the temporal changes are more gradual. When there is a single eddy in the sample region (as in Fig. 6), our stability measure is essentially a measurement of the maximum vertical velocity for that eddy; similar to a local measurement. The apparent difference in unsteadiness between Fig. 6 and Fig. 4(a) is simply due to the fact that there is a single eddy in the case with no electro-osmotic flow.

It is important to note that all parameters are the same as in Fig. 4(a) for the electric field of E=10 000 V/m. In Fig. 4(a) we see very early that the initial conductivity field is unstable, as we find in Fig. 6. However, in Fig. 4(a) where we have electro-osmotic flow, dispersion of the sample region quickly quenches the instability by reducing the magnitude of the conductivity gradients. The dispersive effect of heterogeneous electro-osmosis reduces the susceptibility of the sample to instability by reducing the bulk conductivity gradients. It is clear that instability in the presence of electro-osmotic flow is fundamentally different.

B. 3D flows

Previous studies on electrokinetic instabilities have noted large differences between 2D and 3D instabilities in microchannels [7,15,26,27]. In those studies, the focus was on 3D flows in channels with high aspect ratio. Nevertheless, we must use caution when using 2D simulations to make predictions of what may occur in a real 3D channel. In Fig. 7 we show snapshots of the conductivity field at different instances in time for a 3D geometry. The details of the 3D simulation method can be found in Ref. [26]. The channel is taken to have a square cross section rather than being considered infinite in extent into the page.

These simulations are much more time consuming than their 2D counterparts, therefore extensive numerical parameter studies are currently not practical. While we cannot run extensive tests with the 3D simulation we can use this single simulation to show that the instability is not an artifact of assuming a 2D geometry. Based on this initial result we find that the basic instability mechanism is the same as in the 2D flows. Consistent with previous work, it appears that the threshold for stability is higher in the 3D simulations than in the 2D approximation; note that the applied electric field in Fig. 7 is much higher than in Fig. 2. Further, we note that the time scale for the instability to develop relative to the electro-osmotic time is much greater in the 3D than 2D simulations.

In addition to the quantitative differences, there are some qualitative differences in the conductivity field between the 2D and 3D simulations when we compare the current figure to 3 at the applied field of E_o=35 000 V/m. We see a more regular "vortex street" in the 3D simulation similar to what was observed experimentally by Posner and Santiago [17]. Due to the computational expense of 3D simulations, a thorough study of the difference between 2D and 3D flows is not currently feasible. Our only point in presenting this single result is that the prediction of instability is robust to 3D and the basic mechanism appears unchanged. We would, however, expect to find quantitative differences between the predicted critical electric field based on 2D or 3D simulations.

C. Stability criteria

It does not seem that a simple and rigorous stability criteria can be derived analytically for these flows. In the absence of instability, the two-dimensional conductivity field is unsteady and there is no steady base state about which to perform a linear stability analysis. Even in the absence of instability, our simulations show the flow is very nonlinear due to the heterogeneous boundary conditions at high electric fields. Since analytical progress seems unlikely, we use the 2D simulation to test system stability over a range of parameters.

We vary different parameters of the system including channel height, diffusivity of the electrolyte, conductivity ratio, and ζ-potential. For a given set of parameters we can then vary the electric field to determine (coarsely) a critical electric field. The final stability depends on six dimensionless groups, however some guidance toward a simple criteria for stability is found in the experimental work by Posner and Santiago [17]. It has been found that typically an electric Rayleigh number can be defined which is the most dominant stability parameter when the base state is steady [13,15–17].

We find that for our system, the parameter $\mathrm{Ra}(\gamma-1)$ is most useful for collapsing the data. This is the same critical parameter as used by Baygents and Baldessari [13] who analytically studied instability in the context of isoelectric focusing where the conductivity gradients and electric field are aligned (as in this work). Note that the factor $\gamma-1=(\sigma_{\mathrm{high}}-\sigma_{\mathrm{low}})/\sigma_{\mathrm{low}}$ accounts for the magnitude of the initial conductivity gradient in the flow [17]. In Fig. 8(a) we plot the maximum vertical velocity along the center line over the course

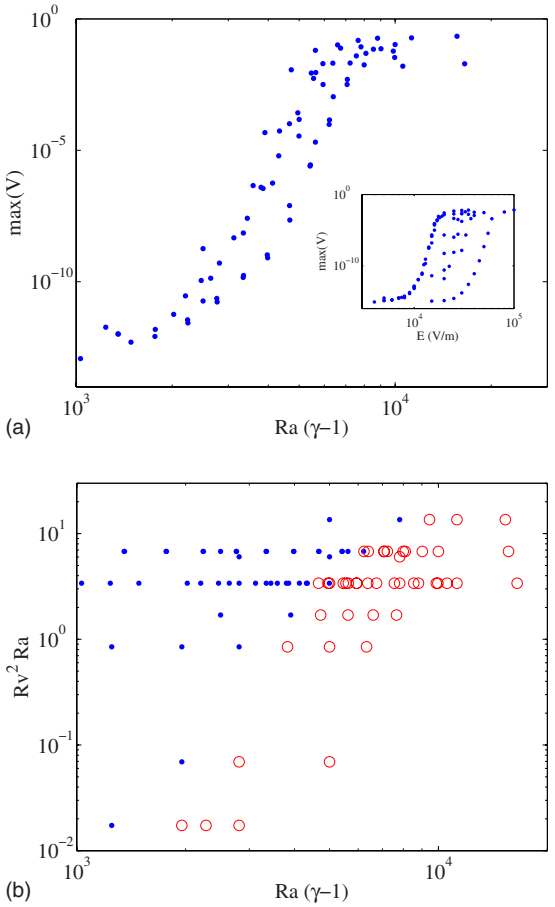

FIG. 8. (Color online) (a) Maximum vertical velocity along the channel centerline during the entire run as a function of Ra$(\gamma-1)$. The dots correspond to 80 different runs with different parameters except all runs have $\zeta=0.07$ V. The different runs varied the electric field, channel height, conductivity ratio, and diffusivity of the electrolyte. The inset shows the same data as a function of the dimensional electric field. (b) Phase diagram showing stable points as blue dots [defined as $\max(V)<10^{-3}$] and unstable points as red circles. There are 110 runs included in this figure.

of the run as a function of Ra$(\gamma-1)$. These cases all have $\zeta_R=0.07$ V, but we vary the electric field, channel height, conductivity ratio, and the diffusivity. We see under this scaling that these points collapse relatively well. In the inset of Fig. 8(a) we show the data in dimensional form to demonstrate the collapse of the data using the dimensionless parameter, Ra$(\gamma-1)$. We note that Baygents and Baldessari found a critical Rayleigh number of Ra=3540 (the factor of 4 difference from their result is due to the domain defined from 0 to H instead of $-H$ to H as we have). Our result shows a critical Rayleigh number of the same order of magnitude, despite a completely different geometry.

If we vary the ζ-potential we find different critical Rayleigh numbers, with higher ζ-potentials corresponding to more stable systems. The reason for this behavior is that as the ζ-potential increases, there is a greater difference between the electro-osmotic slip velocity in the high and low conductivity regions. The internally generated axial pressure gradient increases linearly with the difference in the electro-osmotic velocity of the two regions [11]. Thus, at higher ζ-potentials there is more Taylor dispersion and the instability threshold is pushed higher. While the Rayleigh number characterizes the body forces in the bulk, the second most dominant parameter should clearly be related to the strength of the electro-osmotic flow.

In Fig. 8(b) we show a phase diagram using $R_v^2\,\mathrm{Ra}$ as a second parameter to characterize the dominant stability behavior. The particular scaling is chosen such that the second parameter has no dependence on the applied electric field. The utility of this scaling is seen in Fig. 8(b) where we show 110 runs separated into stable and unstable regions. Of course since the stability depends upon the other dimensionless groups, the stability boundary is not rigorous and is somewhat "fuzzy." However, the data indicate that these two parameters are capable of capturing the dominant stability behavior. While we cannot test over all parameters, we capture a range typical of FASS application from $H=50-100$ μm, $D=5\times10^{-10}-2\times10^{-9}$ m^2/s, $\zeta=0.035-0.14$ V, and $\gamma=2-20$.

Using the definitions of Ra and R_v,

$$R_v^2\,\mathrm{Ra}=\frac{\zeta^2\epsilon}{\mu D}. \tag{16}$$

Recalling the definition of the Rayleigh number earlier in this paper, the above parameter is a Rayleigh number using the ζ-potential rather than the applied potential. This parameter only depends upon the fluid properties and the ζ-potential. The map in Fig. 8(b) is convenient because the choice of electrolyte and the ζ-potential of the system fixes the value of $R_v^2\,\mathrm{Ra}$ and thus the location on the y axis. Once the electrolyte system is chosen, one only needs to compute the Ra$(\gamma-1)$ to estimate the critical electric field.

Finally, we emphasize that the two parameters we have selected for our phase diagram are not unique and our choice can only be considered heuristic. Posner and Santiago [17] review different Rayleigh number scalings as applied by different researchers in previous studies. We can select another of these Rayleigh numbers to separate our data equally into stable and unstable regimes. We proposed Fig. 8 because of the idea that one of the parameters $R_v^2\,\mathrm{Ra}$ is only dependent upon the electrolyte system chosen, not the geometry, electric field, or buffer conductivity. As an example of an alternate, we show a phase diagram with the Rayleigh number scaling proposed by Posner and Santiago [17], namely Ra$(\gamma-1)/\gamma$, in Fig. 9. This figure works equally as well to separate the data. One can construct a number of different alternative scalings and phase diagrams, but at this time we do not have any strong reason to select one choice over another. Therefore, we propose Fig. 8 due to its apparent practical utility.

The striking feature of Fig. 9 is that we see reasonable agreement with Posner and Santiago's experimentally measured critical Rayleigh number of Ra=205, shown as the dashed line. Stability of our system is complicated by the fact that the conductivity field is set by an electro-osmotic flow and therefore depends on other factors than the Rayleigh number. We therefore cannot define a single critical Rayleigh number for our system. However, we have already

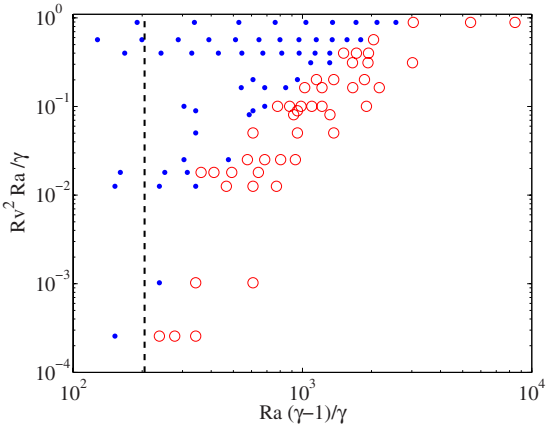

FIG. 9. (Color online) Phase diagram showing stable points as blue dots [defined as $\max(V) < 10^{-3}$] and unstable points as red circles. The data are the same as in Fig. 8, only with different parameters selected for the x and y axis. The experimentally measured critical Rayleigh number of 205 as determined by Posner and Santiago is shown as the dashed line [17].

noted the qualitative similarity between our computed flow structures and the experiments of Posner and Santiago. It appears that using the Posner and Santiago Rayleigh number criteria serves as a reasonable lower bound estimate for instability in our system. That their criteria would serve as a lower bound is reasonable since dispersion can tend to stabilize our system.

D. Conclusions

We have shown that electrohydrodynamic instabilities can occur in microchannels where the fluid conductivity varies in the streamwise direction. Such configurations are common in applications such as field amplified sample stacking which have been developed to increase sample concentration in microfluidics.

We have shown clearly that the resulting unstable flow is due to a complex interaction of the heterogeneous electro-osmotic flow at the channel walls and an electrohydrodynamic instability which occurs in the fluid bulk. While similarities exist between previous work in microfluidic systems, our current work is unique in the strong role that the heterogeneous electro-osmotic flow plays in setting up the conditions for instability. This work extends previous simulations of a similar geometry which did not consider whether the basic flow was stable or not. Due to the unsteady and two-dimensional conductivity field, an analytical determination of system stability should not be expected. Therefore, we use direct numerical simulations of the full nonlinear system to analyze stability. We find that for a given geometry a critical electric field for stability can be found based on whether symmetry is maintained across the channel centerline.

Following previous work on EHD instabilities in microfluidic geometries, we developed a simple two parameter stability map to approximately determine stability. While such a map cannot be exact as the system really depends upon six dimensionless parameters, the two parameter approach is found to work reasonably well.

As we have stated previously, in practice FASS is often conducted with a single interface with semi-infinite plugs of low and high conductivity [4,11]. We can speculate that a similar instability as we observe here would likely occur in the single interface problem if a low conductivity plug is driven into a high conductivity region. However, if a high conductivity plug is driven into a low conductivity region as in the experiments of Refs. [4,11], it is not clear that instability would occur and if it did what the mechanism might be. Going back to Fig. 2 and looking at the trailing edge of the sample region we see that there are no instabilities generated at this location. The instability always occurs at the leading edge where high conductivity fluid is pumped into the center of the sample. Our current numerical scheme assumes our sample traveling in a periodic ring and therefore study of stability of the single interface problem is beyond the current scope. Study of the stability of the single interface problem should provide a rich problem for future study.

In this work we have only considered the motion of the background electrolyte and ignored the behavior of the sample ions. Future work in this area could incorporate the transport of the sample ions to explore how the instability effects the maximum possible stacking concentration. Throughout this work we have also made the assumption that sample ions do not effect the electrical conductivity of the background fluid. In cases where high stacking concentrations are achieved, the concentration of the sample ions may dominate the conductivity of the background electrolyte, further modifying (and complicating) the stability behavior.

Finally, future work should include experimental validation of the numerical predictions presented in this paper. In the absence of such experimental data, we propose the method presented in this paper as an approximate method for determining hydrodynamic stability in two-interface FASS applications. These instabilities should be considered when studying sample transport and dispersion in electrokinetic applications with axial conductivity gradients.

ACKNOWLEDGMENTS

This work was sponsored by the National Science Foundation through Grant No. CTS-0521845. B.D.S. would like to thank Howard Stone.

[1] D. S. Burgi and R. L. Chien, Anal. Chem. **63**, 2042 (1991).
[2] R. L. Chien and D. S. Burgi, Anal. Chem. **64**, 1046 (1992).
[3] S. C. Jacobsen and J. M. Ramsey, Electrophoresis **16**, 481 (1995).
[4] R. Bharadwaj and J. G. Santiago, J. Fluid Mech. **543**, 57 (2005).
[5] R. Probstein, *Physicochemical Hydrodynamics* (Wiley, New York, 1994).
[6] J. G. Santiago, Anal. Chem. **73**, 2353 (2001).
[7] H. Lin, B. D. Storey, and J. G. Santiago, J. Fluid Mech. **608**, 43 (2008).
[8] S. Ghosal, Electrophoresis **25**, 214 (2004).
[9] T. L. Sounart and J. C. Baygents, Colloids Surf., A **195**, 59 (2001).
[10] C. L. Ren and D. Li, J. Colloid Interface Sci. **294**, 482 (2006).
[11] S. Devasenathipathy, R. Bharadwaj, and J. G. Santiago, Exp. Fluids **43**, 959 (2007).
[12] T. L. Sounart and J. C. Baygents, J. Fluid Mech. **576**, 139 (2007).
[13] J. C. Baygents and F. Baldessari, Phys. Fluids **10**, 301 (1998).
[14] A. O. El Moctar, N. Aubry, and J. Batton, Lab Chip **3**, 273 (2003).
[15] H. Lin, B. D. Storey, M. H. Oddy, C.-H. Chen, and J. G. Santiago, Phys. Fluids **16**, 1922 (2004).
[16] C.-H. Chen, H. Lin, S. K. Lele, and J. G. Santiago, J. Fluid Mech. **524**, 263 (2005).
[17] J. D. Posner and J. G. Santiago, J. Fluid Mech. **555**, 1 (2006).
[18] G. I. Taylor and A. D. McEwan, J. Fluid Mech. **22**, 1 (1965).
[19] D. H. Michael and M. E. O'Neil, J. Fluid Mech. **41**, 571 (1970).
[20] J. R. Melcher and C. V. Smith, Phys. Fluids **12**, 778 (1969).
[21] J. F. Hoburg and J. R. Melcher, J. Fluid Mech. **73**, 333 (1976).
[22] J. F. Hoburg and J. R. Melcher, Phys. Fluids **20**, 903 (1977).
[23] J. R. Melcher, *Continuum Electromechanics* (MIT Press, Cambridge, MA, 1981).
[24] R. Jung, R. Bharadwaj, and J. G. Santiago, Electrophoresis **24**, 3476 (2003).
[25] S. Yao and J. G. Santiago, J. Colloid Interface Sci. **268**, 133 (2003).
[26] B. D. Storey, Physica D **211**, 151 (2005).
[27] B. D. Storey, B. S. Tilley, H. Lin, and J. G. Santiago, Phys. Fluids **17**, 018103 (2005).
[28] D. A. Boy and B. D. Storey, Phys. Rev. E **76**, 026304 (2007).